Quantitative comparison of FBP, EM, and Bayesian reconstruction algorithms, including the impact of accurate system modeling, for the IndyPET scanner *

Thomas Frese*,[1], Ned C. Rouze[2], Charles A. Bouman[1], Ken Sauer[3], and Gary D. Hutchins[2]

[1]School of Electrical and Computer Engineering, Purdue University, 1285 ECE Building, West Lafayette, IN 47907-1285, USA, Phone: (765) 494-0340, Fax: (765) 494-3358, Email: {frese, bouman}@ecn.purdue.edu

[2] Indiana University School of Medicine, Imaging Science, Department of Radiology, 541 Clinical Drive, Indianapolis, IN 46202-5111, USA, Phone: (317) 278-7430, Fax: (317) 274-4074, Email: {nrouze,gdhutchi}@iupui.edu

[3]University of Notre Dame, Department of Electrical Engineering, 270 Fitzpatrick Hall, Notre Dame, IN 46556-5637, USA, Phone: (219) 631-6999, Fax: (219) 631-4393, Email: sauer@nd.edu.

Abstract

We quantitatively compare filtered backprojection (FBP), expectation maximization (EM), and Bayesian reconstruction algorithms as applied to the IndyPET scanner, a small to intermediate field of view dedicated research scanner. A key feature of our investigation is the use of an empirical system kernel determined from scans of line source phantoms. This kernel is incorporated into the forward operator of EM and the Bayesian reconstruction algorithms. Our results indicate that, particularly when an accurate system kernel is used, Bayesian methods can significantly improve reconstruction quality over FBP and EM.

1 Introduction

Iterative methods for positron emission tomography (PET) reconstruction can theoretically improve reconstruction quality by modeling the data acquisition process and by regularizing the ill-posed inverse problem. Importantly, iterative methods can achieve significant resolution recovery by incorporating an accurate model of the tomography scanner to account for sinogram blurring due to detector crystal penetration, inter-crystal scatter, depth of interaction and other effects. However, this advantage is often not fully exploited in practical implementations of iterative reconstruction algorithms.

Previous approaches to modeling the tomography scanner for iterative reconstruction have typically relied on analytical modeling of detector properties or on Monte Carlo simulations. Qi, *et al.*, [1, 2] have successfully used such a model for Bayesian reconstruction of data from the microPET and the Siemens/CTI HR+ scanners. Their results demonstrate that accurate modeling in combination with Bayesian reconstruction algorithms can give superior resolution and ROI quantitation at lower variance as compared to FBP and OSEM.

In this study, we quantitatively compare FBP, EM, and Bayesian reconstruction algorithms and evaluate the impact of modeling the scanner for iterative reconstruction. Our results are based on phantom data acquired on the IndyPET tomography scanner[3], and also on simulated data. In contrast to previous approaches, we have obtained a system kernel for the IndyPET scanner empirically using scans of line source phantoms. This empirical approach is greatly simplified by the non-circular detector geometry of the scanner which allows for measuring the full range of incident photon angles using only sources positioned near the center of the field of view. For the iterative reconstruction methods, we compare reconstruction quality for our empirical kernel and a simple triangular kernel calculated based on detector solid angle.

For the Bayesian reconstruction algorithms, we compare three different prior models; a Gaussian Markov random field (GMRF), a generalized Gaussian Markov Random field (GGMRF)[4] and a wavelet prior model[5]. Furthermore, we evaluate a modification of Bayesian methods proposed by Fessler and Rogers[6] that produces reconstructions with approximately uniform resolution.

2 IndyPET Scanner

As illustrated in Fig. 1, the distinguishing feature of the IndyPET scanner[3] is the use of two, approximately planar detector banks with adjustable separation which are mounted on a rotatable gantry. Each detector bank consists of 8 CTI-HR BGO detector modules whose crystals are cut into a 7 (transaxial) by 8 (axial) array of segments

*This work was supported by the National Science Foundation under Grant MIP97-07763, the National Cancer Institute under Grant ICMIC P20-CA86350-2, and the State of Indiana 21st Century Research and Technology Fund "Indiana Center of Excellence in Biomedical Imaging".

0-7803-7324-3/02/$17.00 © 2002 IEEE

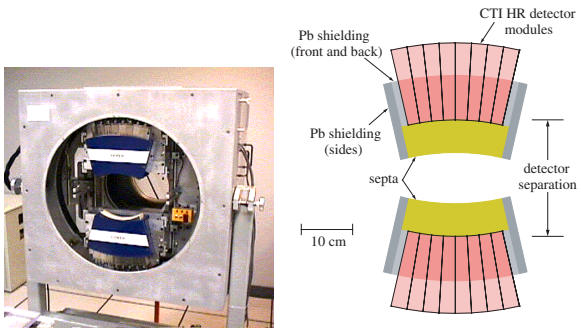

Figure 1: Photograph and detector geometry of the IndyPET scanner.

with a transaxial spacing of 3.3 mm and an axial spacing of 6.3 mm. The crystal depth is 30 mm.

In comparison to using a full ring of detectors, the scanner's geometry results in reduced parallax and approximately uniform resolution throughout the field of view. However, because the detectors do not form a full ring, data must be collected at multiple gantry positions.

To model the system kernel, we consider the projection matrix P such that P_{ij} is proportional to the probability that an emission from pixel j is registered by the i^{th} detector pair. Assuming that pixels in the reconstruction image are considerably smaller than the detectors, P_{ij} can be written as

$$P_{ij} \approx h_i(s_{c_j})A_j \tag{1}$$

where $h_i(s)$ is the kernel of the i^{th} detector pair, s is the coordinate, s_{c_j} is the center coordinate of pixel j, and A_j is the area of pixel j. We assume that the factor $h_i(s)$ depends only on the projection angle θ_i relative to the detectors and the displacement $\Delta t_{s,i}$ of location s from the ideal projection line connecting the centers of detector pair i. Then we model $h_i(s)$ as

$$h_i(s) = h(\theta_i, \Delta t_{s,i}) \tag{2}$$

where we call the 2-D function h the *system kernel*. The simplicity of the parameterization (2) is a direct consequence of the use of approximately plane detector banks in the IndyPET scanner. In contrast, the parameterization for a circular detector geometry would require an additional parameter since the detector orientation relative to the projection lines is a function of the displacement of the projection from the center of the field of view.

We measured the system kernel $h(\theta_i, \Delta t_{s,i})$ using an axially oriented line source phantom stepped through the center of the field of view. The measured counts were corrected for detector efficiencies and parameterized by projection angle θ and displacement difference $\Delta t_{s,i}$ between the needle position s and the ideal projection line. The resulting empirical system kernel $h(\theta, \Delta t)$ is shown in Fig. 2. We observe that the response is wider and more complicated than for a simple triangular response profile based on solid angle. Also, the result in Fig. 2 does not indicate a significant dependence on projection angle due to the limited range of projection angles acquired with the IndyPET scanner.

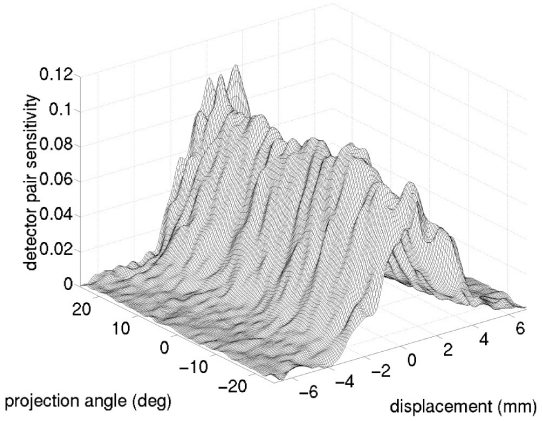

Figure 2: Meshplot showing the empirical system kernel $h(\theta, \Delta t)$ for the IndyPET scanner. The kernel is parameterized by projection angle θ and the displacement Δt of the source from the ideal projection line.

3 Reconstruction Algorithms

We compare reconstructions obtained using FBP, EM, and Bayesian techniques with three different prior models. For EM and the Bayesian methods, the exact Poisson counting statistics were used to model the data acquisition. Transmission attenuation coefficients were calculated by forward projecting the estimated support of the imaged object using a constant attenuation coefficient. Scatter and randoms correction factors were estimated directly from the sinogram. For the Bayesian methods, we compare three different prior models; a Gaussian Markov random field prior (GMRF), a generalized Gaussian Markov random field (GGMRF)[4] prior and an adaptive wavelet graph model (WGM) prior. The GGMRF was proposed in as an edge-preserving MRF prior with a convex potential function. For our experiments, we chose a GGMRF shape parameter of $p = 1.5$. The adaptive wavelet graph model (WGM)[5] is a nonlinear prior model formulated in the wavelet domain and exploits dependencies between wavelet coefficients at different resolutions. For the results presented here, the WGM model was implemented and trained as described in [5]. The MAP optimization for all three prior models was performed using the iterative coordinate descent (ICD) algorithm[4, 7].

Reconstructions were performed as a function of a smoothing parameter appropriate for each reconstruction

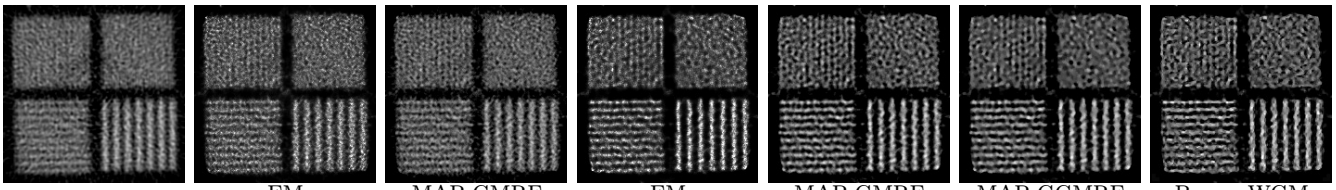

FBP ramp flt. | EM triangular kernel | MAP GMRF triangular kernel | EM empirical kernel | MAP GMRF empirical kernel | MAP GGMRF empirical kernel | Bayes. WGM empirical kernel

Figure 3: Bar phantom reconstructions with smoothing parameters selected to minimize the expected error for the bar profiles in quadrant 3 (2.90 mm bars). The field of view is 13.50 × 13.78 cm at a resolution of 0.70 mm/pixel.

method. For FBP, the cutoff frequency of a Hanning filter was varied. For EM, the number of iterations was varied. For the Bayesian methods, the scale parameter of the prior was varied.

4 Experimental Results

Reconstruction quality for different combinations of reconstruction algorithms and system kernels was analyzed using two sets of phantom data collected on the IndyPET scanner and using a simulated data set containing a circular lesion on an approximately uniform background. For the phantom data sets, we performed EM and Bayesian reconstructions using the empirical system kernel shown in Fig. 2 and using a triangular kernel of width 3.3 mm which is the analytical result based on solid angle.

4.1 Bar Phantom

The bar phantom consists of four arrays of parallel acrylic bars with thicknesses of 1.55, 2.31, 2.90, and 4.32 mm separated by gaps of equal widths, resulting in square wave emission profiles with different periods for each quadrant. The data set acquired on the IndyPET scanner contained 10.4M counts in the 2-D reconstruction plane.

Figure 3 shows sample reconstructions with the smoothing parameters chosen to minimize the expected spatial reconstruction error (see below) for the 2.90 mm bars in quadrant 3. Based on visual inspection, the empirical system kernel significantly improves the quality of the iterative reconstruction techniques. Also, when the empirical system kernel is used, the iterative techniques provide improved resolution over FBP. For the Bayesian reconstructions, the non-Gaussian GGMRF and WGM prior models provide sharper edges as compared to the GMRF prior. However, the GMRF prior appears to have a wider frequency response, allowing for good reconstruction quality of all quadrants using a single regularization parameter.

The bar phantom reconstructions were analyzed quantitatively by comparing the reconstructed signal to the expected square wave profile. Bias and variance measures were computed separately for each quadrant Q by fitting a harmonic series to the reconstructed bar profiles averaged over the coordinate parallel to the bars. The bias is given by

$$\text{bias}_Q^2 = \min_c \left\{ \sum_{k=1}^{K} \left(\frac{a_k}{c} - \alpha_k \right)^2 + \sum_{k=0}^{K} \left(\frac{b_k}{c} - \beta_k \right)^2 \right\} . \tag{3}$$

where a_k and b_k are coefficients of the fitted sine and cosine terms, c is a scaling parameter, and α_k and β_k are the coefficients of an ideal square wave. The variance was calculated between the reconstructed pixel values x_i and the fitted values $\tilde{x}_i$,

$$\text{var}_Q = \text{std}_Q^2 = \frac{1}{c^2(N_i^2 - 1)} \sum_i (x_i - \tilde{x}_i)^2 \tag{4}$$

where N_i is the number of pixels.

Figure 4 shows bias versus standard deviation separately for the three quadrants. The curves were obtained by varying the smoothing parameter for each reconstruction method. The plots indicate that the empirical system kernel significantly lowers the bias at equal variance for EM and Bayesian GMRF MAP. Specifically, when the triangular kernel is used, EM and GMRF MAP perform similarly. In this case, the iterative methods do not outperform FBP in the low variance region. However, when the empirical kernel is used, GMRF MAP achieves significantly lower bias at equal variance as compared to EM. In this case, both EM and the Bayesian methods perform significantly better than FBP. Note, that the FBP reconstructions have low variance and high bias even for a ramp filter since no resolution recovery is performed.

4.2 Hoffman 3-D Brain Phantom

The Hoffman 3-D brain phantom data set acquired on the IndyPET scanner contained 2M counts in the 2-D reconstruction plane. Figure 5 shows reconstructions for the different algorithms and system kernels. In general, using the empirical kernel significantly improves the quality of the EM and MAP GMRF reconstructions. For the empirical kernel, the EM result does not reproduce the interior contours as well as the Bayesian techniques. As compared to the GMRF, the GGMRF prior produces sharper contours with few artifacts. The WGM produces a much sharper image, however, the result has significant artifacts.

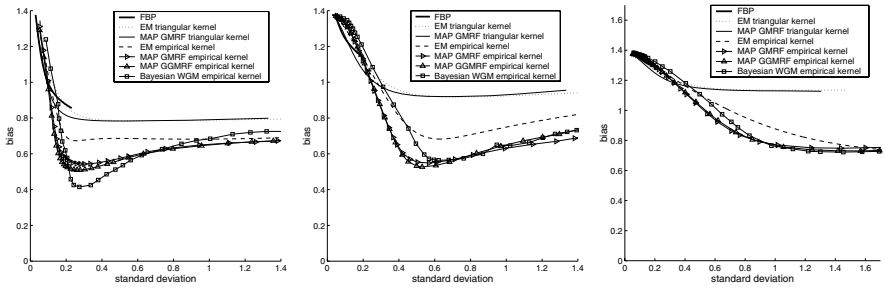

quadrant 4, 4.32 mm bars quadrant 3, 2.90 mm bars quadrant 2, 2.31 mm bars

Figure 4: Plots of bias versus standard deviation for the bar phantom reconstructions.

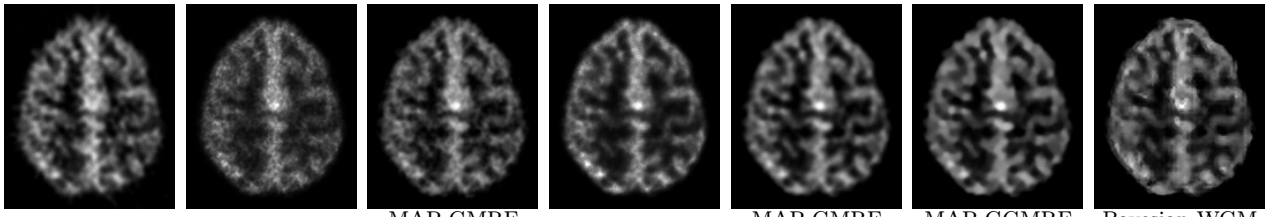

FBP EM triag. MAP GMRF triag. EM emp. MAP GMRF emp. MAP GGMRF emp. Bayesian WGM emp.

Figure 5: Reconstructions of Hoffman 3-D brain phantom.

4.3 Simulated Lesion Phantom

Simulated projection data were generated using the image shown in Fig. 6(a) containing a constant circular lesion of 4 mm diameter added to an approximately uniform background. The amplitude of the lesion was 5 times the background activity.

Twenty noisy realizations of simulated projection data were generated by forward projecting the image shown in Fig. 6(a) using the empirical system kernel and adding Poisson noise corresponding to 130,000 counts in the reconstruction plane. For the iterative reconstruction methods, only the empirical system kernel was used. Even though the use of the same system kernel for forward projection and reconstruction will bias the results towards the iterative reconstruction techniques, we still obtain fair comparisons between different iterative techniques and obtain an approximate idea about their performance relative to FBP.

The reconstructions were analyzed quantitatively by calculating the errors e_L^2 and e_B^2 given by

$$e_L^2 = \frac{1}{\mu_L^2 N_L} \sum_{j \in L} (\hat{x}_j - x_j)^2 \tag{5}$$

and

$$e_B^2 = \frac{1}{\mu_B^2 N_B} \sum_{j \in B} (\hat{x}_j - x_j)^2 \tag{6}$$

where x_j and $\hat{x}_j$ are pixel values in the ground truth and reconstructed images, μ_L and μ_B be the true mean activity values, and N_L and N_B are the number of pixels

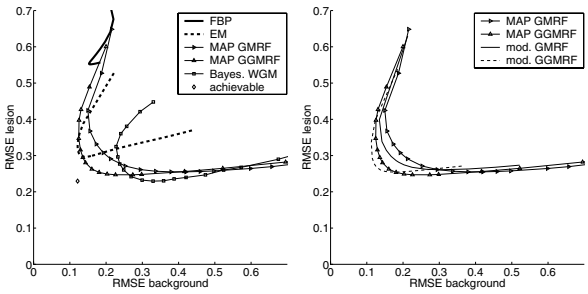

(a) (b)

Figure 6: Plots of lesion RMSE versus background RMSE for reconstructions of the simulated lesion phantom. Shown in (a) is a comparison for the different iterative methods and FBP. Shown in (b) is the effect of using the modification of the MAP prior proposed in [6].

in the respective regions. The errors e_L^2 and e_B^2 are averaged over the 20 reconstructions of the different noise realizations to give estimates $\hat{E}[e_L^2]$ and $\hat{E}[e_B^2]$ for the expected relative errors for each reconstruction method as a function of regularization parameter.

Figure 6(a) shows a plot of the expected reconstruction error $\sqrt{\hat{E}[e_L^2]}$ for the lesion versus the expected reconstruction error $\sqrt{\hat{E}[e_B^2]}$ for the background for different algorithms. The curve for each algorithm was obtained by varying the smoothing parameter. We observe that for the lesion region, the Bayesian methods achieve lower error compared to EM. Also, the GGMRF prior model performs significantly better than the GMRF prior since

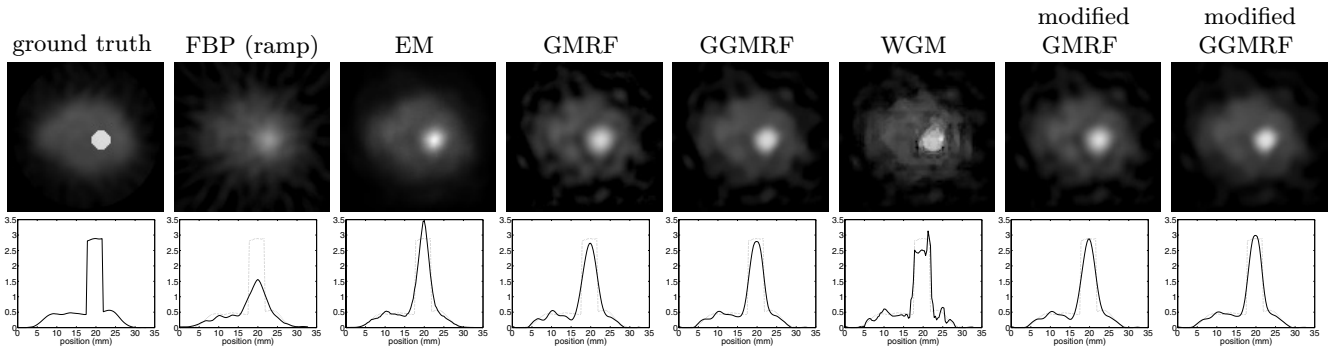

Figure 7: Reconstructions of the simulated tumor phantom. The 1-D profiles correspond to a single row of pixels intersecting the center of the lesion.

the GGMRF curve reaches a point closer to the coordinate origin, signifying lower combined error.

Figure 6(b) shows the reconstruction error for Bayesian GMRF and GGMRF reconstructions using the modification proposed by Fessler and Rogers[6]. This modification is effective in reducing the combined lesion and background errors since the curves move closer to the coordinate origin. However, the minimum error in the lesion region is slightly higher for the modified priors.

Figure 7 shows reconstruction images as well as 1-D profiles through the lesion for the different algorithms. For the iterative reconstructions, the results in Fig. 7 correspond to the value of smoothing parameter that minimizes the combined error ($\hat{E}[e_L^2] + \hat{E}[e_B^2]$); for FBP, a ramp filter reconstruction is shown. We observed that the iterative algorithms resolve the lesion substantially better than FBP. In comparison to EM, the Bayesian GMRF and GGMRF reconstructions more accurately quantify the lesion. The WGM prior model segments the lesion surprisingly accurately, however, it slightly underestimates lesion activity and has some artifacts. Overall, the modified GGMRF model appears to achieve the most accurate result. Note that the reconstructions have ringing artifacts in the background due to the extremely high reconstruction resolution which is consistent with observations in earlier studies[1].

5 Conclusions

We have presented a comparison of reconstruction quality for FBP, EM, and Bayesian algorithms as implemented for the IndyPET scanner. A key feature of this investigation is the determination of an empirical system kernel based on scans of line source phantoms which may be simpler and potentially more accurate than modeling of detector properties and Monte Carlo simulations.

For the data sets and evaluation methods used in this study, we found that without an accurate system kernel, the reconstruction quality of the iterative methods was similar to that of FBP. However, when an accurate system kernel was incorporated, Bayesian MAP techniques were superior to EM and EM was superior to FBP.

Acknowledgment

We thank Robert Koeppe, Ph.D., of the University of Michigan for supplying the Hoffman 3-D brain phantom.

References

[1] J. Qi, R. M. Leahy, S. R. Cherry, A. Chatziioannou, and T. H. Farquhar. High-resolution 3D Bayesian image reconstruction using the microPET small-animal scanner. *Phys. Med. Biol.*, 43(4):1001–1013, April 1998.

[2] J. Qi, R. M. Leahy, C. Hsu, T. H. Farquhar, and S. R. Cherry. Fully 3D Bayesian image reconstruction for the ECAT EXACT HR+. *IEEE Trans. on Nuclear Science*, 45(3):1096–1103, June 1998.

[3] N. C. Rouze, W. Winkle, and G. D. Hutchins. IndyPET - a high resolution, high sensitivity dedicated research scanner. In *Proc. of IEEE Nucl. Sci. Symp. and Med. Imaging Conf.*, volume 3, pages 1460–1464, Seattle, WA, October 24-30 1999.

[4] C. A. Bouman and K. Sauer. A generalized Gaussian image model for edge-preserving MAP estimation. *IEEE Trans. on Image Processing*, 2(3):296–310, July 1993.

[5] T. Frese, C. A. Bouman, N. C. Rouze, G. D. Hutchins, and K. Sauer. Bayesian multiresolution algorithm for PET reconstruction. In *Proc. of IEEE Int'l Conf. on Image Proc.*, pages 613–616, Vancouver, BC, Canada, September 10-13 2000.

[6] J. A. Fessler and W. L. Rogers. Spatial resolution properties of penalized-likelihood image reconstruction: Space-invariant tomographs. *IEEE Trans. on Image Processing*, 5(9):1346–1358, September 1996.

[7] C. A. Bouman and K. Sauer. A unified approach to statistical tomography using coordinate descent optimization. *IEEE Trans. on Image Processing*, 5(3):480–492, March 1996.